Chapter 7

Interaction Region

7.1 Beam Line Layout

The design beam parameters of KEKB and their rationale have been discussed in Chapter 1. Some pertinent parameters are repeated in Table 7.1 for convenience.

A schematic layout of the beam line near the interaction point (IP) is shown in Figure 7.1. The figure shows the following magnets: S-R, QCS-R, QC1ER, S-L, QCS-L and QC1EL. The final vertical focusing of two beams is provided by a pair of superconducting quadrupole magnets, QCS-R and QCS-L. The superconducting solenoid magnets, S-R and S-L, are for compensating solenoid fields created by the detector facility. The QCS and S magnets on each side of the interaction point (IP) are contained in a common cryostat enclosure.

The vertical focusing field strength of QCS is tuned to the positron energy (3.5 GeV). Extra vertical focusing for the electron (8.0 GeV) is provided by a pair of normal conducting quadrupole magnets QC1E-L and QC1E-R. The beam separation and the geometry of QC1E magnets are designed such that only the electrons would see non-zero gradient fields when passing through them. To minimize the growth of chromaticity from this region, the QC1E magnets are placed close to the QCS magnets, in as much as the hardware design constraints allow.

The positrons enter the IP through QCS-R and leave the IP through QCS-L. The electrons proceed in the opposite direction. Since the two beams collide at the IP at a finite crossing angle of 2×11 mrad, inevitably one beam or the other must go off axis within the QCS. To minimize the flux of synchrotron radiation through the IP, the incoming positron beam orbit is set on the axis of QCS-R. Likewise, the incoming electron beam is set on the axis of QCS-L.

A sufficiently large beam separation is created at QC1E-L, so that a full quadrupole

	LER	HER	
Energy	3.5	8.0	GeV
Crossing angle	± 11		mrad
Luminosity	1×10^{34}		$\mathrm{cm}^{-2}\mathrm{s}^{-1}$
Tune shifts (ξ_x/ξ_y)	0.039/0.052		
Beta function (β_x^*/β_y^*)	0.33/0.01		m
Beam current	2.6	1.1	A
Bunch length	4		mm
Energy spread	7.1×10^{-4}	6.7×10^{-4}	
Bunch spacing	0.59		m
Particles/bunch	3.3×10^{10}	1.4×10^{10}	
Emittance ($\varepsilon_x/\varepsilon_y$)	$1.8 \times 10^{-8}/3.6 \times 10^{-10}$		m
Synchrotron tune	0.01∼0.02	0.01∼0.02	
Betatron tune (ν_x/ν_y)	45.52/45.08	47.52/43.08	

Table 7.1: Beam parameters related to the IR issues.

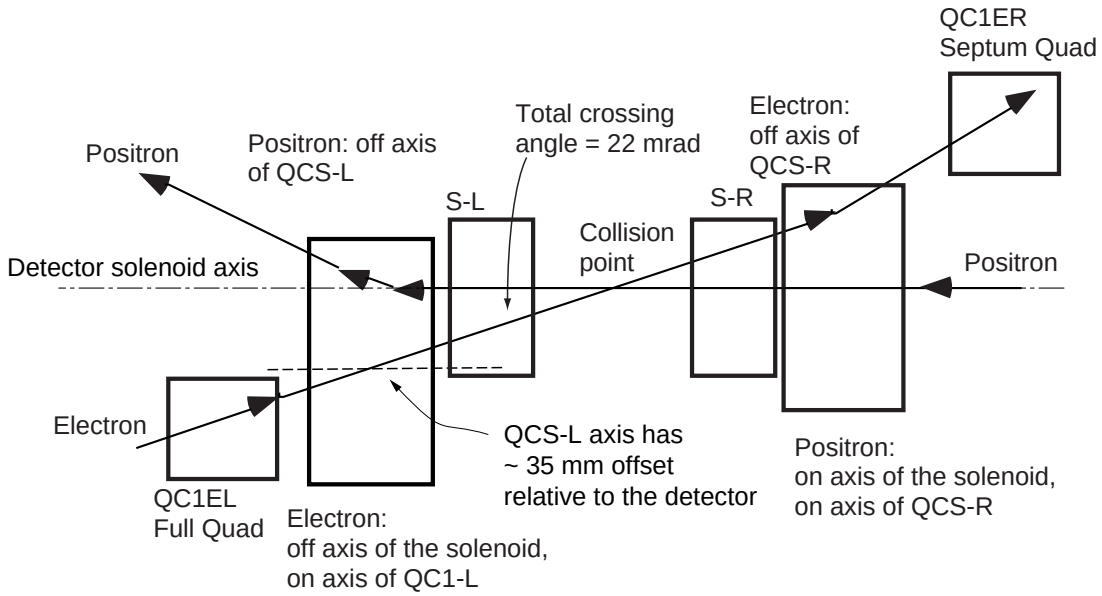

Figure 7.1: Schematic plan view layout of the magnets and the beam line near the interaction point. The superconducting solenoid S-R and the final focusing quad QCS-R are contained in a single cryostat. Similarly, S-L and QCS-L are contained in another cryostat.

Magnet	Detector solenoid	Electron	Positron
S-L	On axis		
QCS-L	Off axis	Incoming	Outgoing
	by -35 mm	on axis of QCS-L	off axis of QCS-L
S-R	On axis		
QCS-R	On axis	Outgoing	Incoming
		off axis of QCS-R	on axis of QCS-R

Table 7.2: Required transverse alignment of the QCS and S magnets relative to the detector solenoid and the beams.

magnet can be built for the incoming electrons to pass through its center. This is an important step to minimize the synchrotron radiation emitted by the electrons, which naturally propagates towards the IP. At the same time, magnetic perturbations to the outgoing positrons is minimized.

The orientation of the beam line relative to the detector solenoid field axis has been chosen, such that the incoming positron through QCS-R is on the axis of the detector solenoid. Because of the crossing angle, this means that the incoming electrons through QCS-L will be off-axis of the detector. This is the preferred arrangement based on considerations on the detector geometry. Since the QCS-R side is where the electrons (i.e. high energy beam) leave the IP, the detector facility would like to occupy a solid angle coverage closer to the beam line, compared to the QCS-L side. This means that a smaller space would be available for the QCS-R cryostat. If the QCS-L is aligned relative to the detector solenoid axis, the required aperture for QCS-R become larger, because the field axis of QCS-R cannot be in line with the detector solenoid axis. This leads to an increased exterior cryostat size for the QCS-R, which, in turn, would conflict with the detector solid angle coverage.

The compensation solenoid magnets S-R and S-L will have their field axis aligned to the detector solenoid. The relative transverse alignments of those superconducting magnets are summarized in Table 7.2.

The first horizontal focusing will be provided by the QC2 magnets, as shown in Figure 7.2. Like the QC1 magnets, iron-dominated normal conducting magnets will be used as QC2's. Their inner aperture shapes are designed so that either only an electron or positron beam will see the desired focusing field.

The locations of the QCS, QC1 and QC2 magnets and their field gradient values are summarized in Table 7.3. The distance z along the beam line from the IP is denoted

with positive values in the "right" direction, where the electron leaves the IP. The "left" direction, where the electron enters the IP, is denoted by negative values of z.

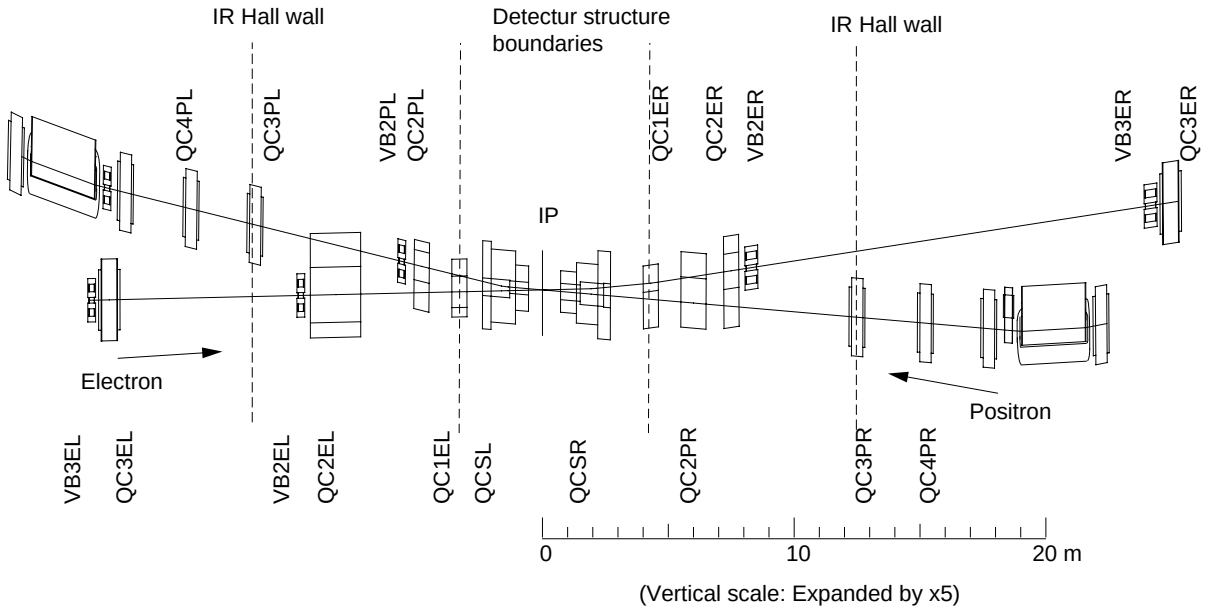

Figure 7.2: A schematic diagram of the beam line beyond QC1 magnets.

Magnet	Z_{min} (m)	$Z_{max}(m)$	Field gradient (T/m)	Purpose
QC2E-L	-8.0	-7.2	5.78	Horiz. focusing e^-
QC2P-L	-5.0	-4.4	6.42	Horiz. focusing e^+
QC1E-L	-3.6	-3.0	-14.6	Vert. focusing e^-
QCS-L	-1.85	-1.35	-16	Vert. focusing e^-e^+
QCS-R	1.685	2.185	-16	Vert. focusing e^-e^+
QC1E-R	4.0	4.6	-14.47	Vert. focusing e^-
QC2P-R	5.4	6.4	3.9	Horiz. focusing e^+
QC2E-R	7.2	7.8	9.7	Horiz. focusing e^-

Table 7.3: Positions relative to the IP and field gradients of the QCS, QC1 and QC2 magnets.

Several orbit correction dipole magnets will also be installed in the beam line. A few horizontal and vertical bend magnets are required to match the orbit to the rest of the straight section. As discussed in Chapter 2, local chromaticity corrections are

applied to the LER in the straight section that includes the IR. A schematic beam line layout of the IR, including a part of the chromaticity correction sections, is shown in Figure 7.3. Soft bend magnets will be used as the last dipole magnets for the incoming beam to see before reaching the IP. This is so that the critical energy of synchrotron radiation off these magnets will be sufficiently low, and that it would not cause harmful background to the detector facility.

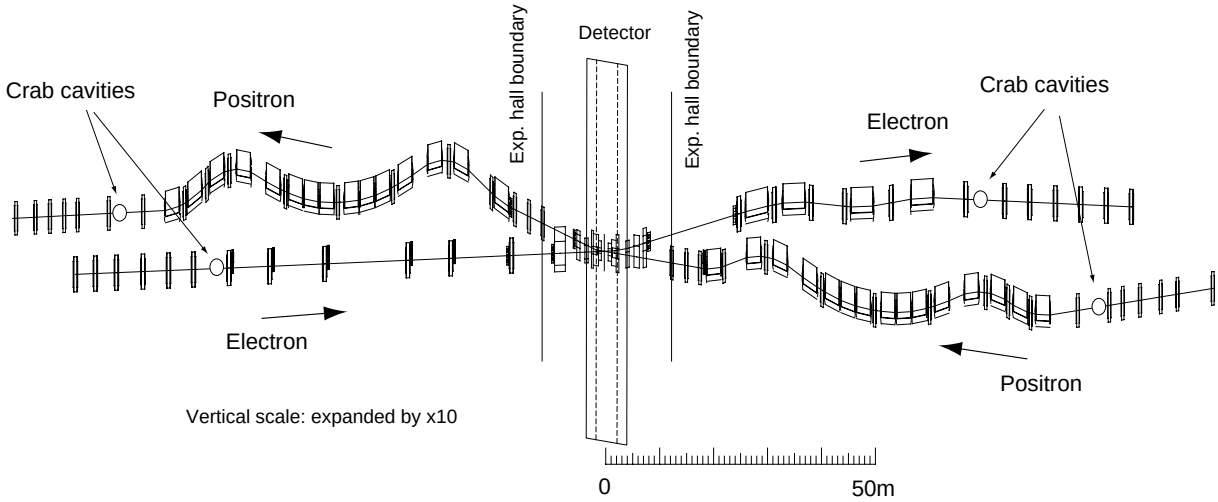

Figure 7.3: Schematic layout of the HER and LER beam lines in the straight section which includes the IR. Part of the LER local chromaticity corrections are shown.

Although the bulk of the x-y coupling effects due to the detector solenoid are cancelled by compensation solenoids S-L and S-R, the remaining coupling terms need to be corrected in the rest of the IR beam line. For this purpose, the support frames for QC1, QC2, QC3 and several other magnets allow us to introduce a variable amount of small rolls ($< 2^\circ$) for introducing skew components to the magnetic field. The roll angles will be remotely controlled using a magnet mover mechanism. Engineering development of these magnet support will begin soon.

7.2 Detector Boundary Conditions

7.2.1 Geometric Conditions

The detector facility for high energy physics experiments at KEKB has approximately an axially symmetric geometry around the beam line. Physics requirements call for a good solid angle coverage for detecting decay product particles from $e^+e^- \to B\overline{B}$ interactions. Figure 7.4 shows a schematic side view of the proposed detector facility.

Table 7.4 summarizes the solid angle coverage requested by proponents of the detector facility. In the table, the polar angle is measured from the forward extreme, i.e.

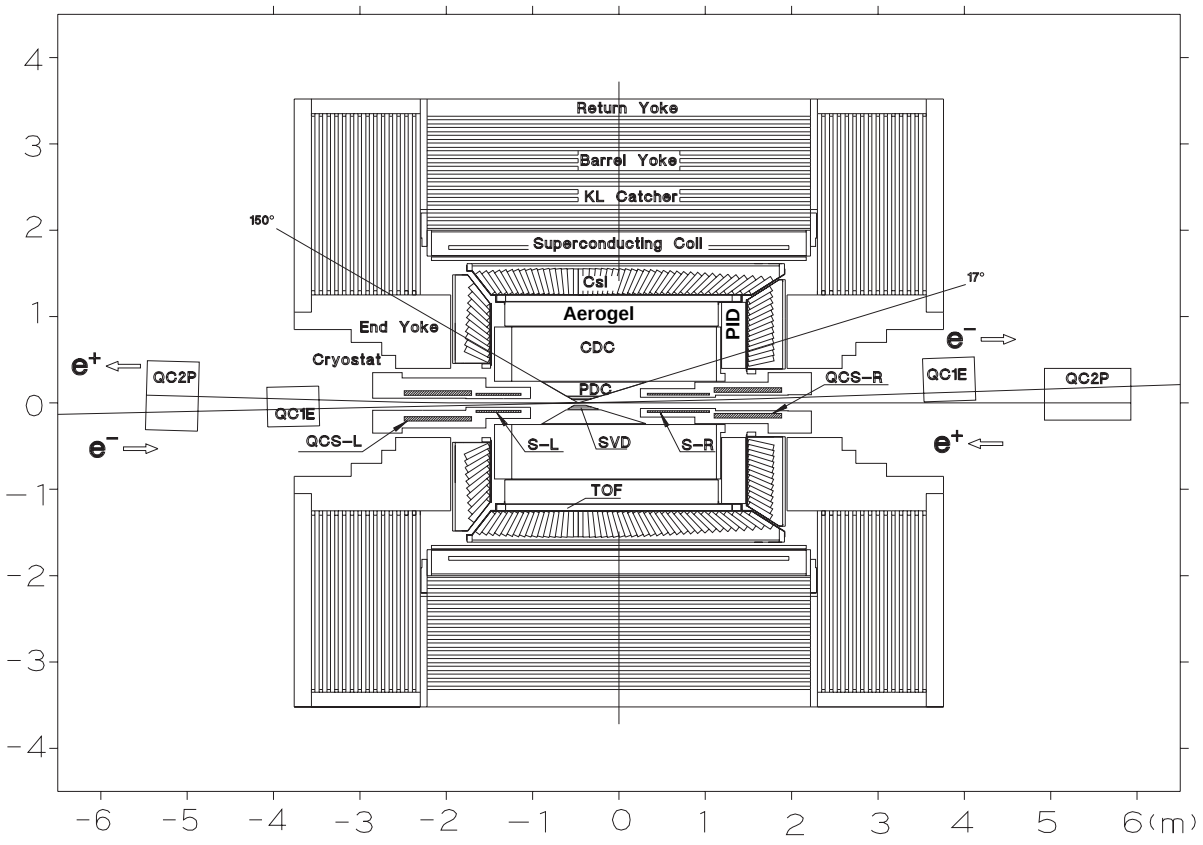

Figure 7.4: Schematic side view of the proposed detector facility, together with the accelerator cryostat for superconducting compensation solenoid and QCS magnets. A pair of normal conducting quadrupole magnets and QC1EL and QC1ER are also shown. Details of the detector configuration may vary in the final design.

Detector	Polar angle range
Barrel K_L catcher and μ detector	45° - 113°
Forward K_L catcher and μ detector	25° - 45°
Backward K_L catcher and μ detector	113° - 155°
Barrel Calorimeter	32.5° - 130°
Forward Calorimeter	11.5° - 32.5°
Backward Calorimeter	130° - 160°
Barrel TOF/TSC	32.5° - 130°
Barrel Particle ID device	32.5° - 130°
Forward Particle ID device	12.5° - 32.5°
Central Drift Chamber	17° - 150°
Silicon Vertex Detector	17° - 150°

Table 7.4: Polar angle coverage requested by the experimental detector facility.

the direction where the positrons enter the interaction point (IP).

The interaction point relative to the detector center is shifted towards the left by 470 mm. This is for increasing the solid angle coverage in the forward direction, while taking into account the Lorentz boost of the final state particles in the asymmetric collision.

The detector geometry that has a direct bearing on the accelerator design is that of the central drift chamber (CDC). In the latest design the CDC has an inner radius of 280 mm. Thus, the accelerator components must fit within a cone-shaped space with an opening angle of 17 degrees forward and 30 degrees backward, clipped by the CDC inner radius, minus the cable space for detector elements. The CDC occupies the Z space between -970 mm and $+1660$ mm, as measured from the IP.

Just at the IP, a high precision particle tracking device based on silicon micro strips will be installed. Its design calls for a small vacuum chamber around the IP with an inner radius of 20 mm for $-80 < Z < +80$ mm. The particle trajectories during the injection period and synchrotron radiation during the run must not be intercepted by this aperture.

7.2.2 Magnetic Conditions

The nominal solenoid field created by the detector magnet for charged particle tracking is 1.5 T. The field is extended in an effective volume length of $\sim \pm 2.5$ m. If the solenoid field of the detector is not cancelled in situ on the beam line, its coupling

effects must be corrected by using a set of skew quadrupole magnets, whose strength is approximately $K_{SQ} \approx 0.05$. However, corrections with skew quad magnets are exact only for on-energy particles. The remaining chromatic coupling term will result in an increased vertical emittance. Also, the use of skew quadrupole magnets will create extra chromaticity, which need to be compensated in chromaticity correction sections in the arcs and elsewhere. This tends to reduce the available dynamic aperture, and consequently, the expected beam lifetime. Furthermore, there is an indication from simulations on beam-beam effects, that the luminosity will tend to be reduced if the solenoid field compensation is not sufficient.

Beam dynamics calculations have been conducted to evaluate these effects. Cases with various sophistication of solenoid field compensation schemes have been examined. It has been found that if *the integral of the axial field B_z is cancelled to zero on the average*, the reduction of the dynamic aperture and its effects on the beam lifetime are negligible. In that condition, the accelerator performance is comparable to the case where the detector solenoid field is completely absent. The effects of fringe fields of the solenoid and quadrupole magnets are taken into account. As an example of incomplete field compensation, in the case with a left-over field of $\int B_z dz = 1.5$ T m, it has been found that up to a 30% reduction of the beam lifetime will result, because of the reduced dynamic aperture. Thus, the goal of field compensation for the accelerator within the detector volume should be to bring the *net value* $\int B_z dz$ to zero. The superconducting compensation solenoid magnets S-L and S-R will be implemented to achieve this.

Magnetic fields from S-L, S-R, QCS-L and QCS-R will leak into the detector volume, and distorts its solenoid tracking field. Their effects in physics analyses were a potential problem. Simulation work by the detector group has shown that the effects of the leak field due to S-L and S-R magnets are, in fact, manageable. Relatively straightforward tuning of the track analysis software can recover the full momentum resolution of charged particles. It has been also found that perturbations due to leak fields from QCS magnets are sufficiently isolated from the interaction point. In addition, the quadrupole field component quickly attenuates as a function of r, the radial distance from the beam line. Thus, the leak quad field is also manageable from the physics analysis view point. Therefore, no additional compensation magnets will be implemented to shield the detector volume from S and QCS accelerator magnets.

Since QCS-L is not in line with the detector axis, the field that is produced by QCS-L may couple with the detector iron in such a way as to create an axially non-symmetric field on the accelerator beam line. The magnitude of such multipole fields has been evaluated, and its effect on the beam dynamics examined. It has been found that their adverse effects are negligible. Consequently, no special measures will be

taken to shield QCS from the detector iron structure, either. However, it is felt that in any case it is desirable to introduce some correction devices for multiple pole field errors. A feasibility study of such devices is now being prepared.

Turning to outside the QCS region, the QC1E-L and QC1E-R magnets will be located near the outer edge of the detector structure. If the magnetic field from the detector solenoid is large there, the presence of QC1E iron can significantly distort the magnetic field near their entrance. Unless care is taken, this will lead to sizeable multipole field errors to be felt by the beams.

The magnitude of the detector leak field depends on the details of the relative geometry of the detector and the accelerator. There is a desire on the part of experimental physicists to increase the thickness of the end yoke for better muon detection coverage. This would tend to increase the leak field from the detector, unless care is taken to reduce the magnetic saturation within the detector structure. Or, both the accelerator and detector designers agree that increasing the inner aperture size of the detector end cap (currently set to be 1000 mm diameter) would relax the space problem for cabling, installation and maintenance. However, it would quickly increase the detector leak field.

In one version of the structure design, the detector leak field near QC1E could be reduced to $B_z < 20$ G and $B_r < 20$ G, which is considered to be acceptable from a beam dynamics viewpoint. Efforts are still on-going to optimize the structure configuration so that the detector coverage is maximized while the leak field is minimized. Preparations for high-precision 3-dimensional field calculations in this area are in progress. A possible use of weak compensation solenoid magnets or end-shimming is also being considered near QC1 magnets. However, the priority is on efforts to first reduce the strength of the detector leak field.

7.3 Beam Line Aperture Considerations

The aperture of the vacuum chambers in the QCS and S magnets have been determined, so that neither the beam during injection time nor the synchrotron radiation (SR) during the data acquisition time should directly hit the inner surface of the vacuum pipes.

The beam envelope considered in the injection system design is 1.2×10^{-5} m for x and 1.2×10^{-6} m for y. To include a safety margin, in the design of IR the beam envelope emittance of 2×10^{-5} m for x and 2×10^{-6} m for y is assumed. Parallel to these, the trajectories of SR photons from 10σ particles during the collision time have been calculated. The beam stay clear values have been determined from the maximum

of the injection time beam envelope and the run-time SR flux trajectory. This beam stay clear, plus 13 mm for the work space for the vacuum chambers is specified as the required inner aperture of the cryostats for QCS and S magnets.

The beam stay clear for QC1 and QC2 magnets has been determined by considering only the injection condition. The assumed beam envelope is 1.4×10^{-5} m for x and 2×10^{-6} m for y.

The vacuum chamber that connects the beam line between those magnets must fully contain the specified beam-stay clear. Since the β function values are rapidly changing in this area, the beam stay clear also varies along the beam line. The design of the vacuum chamber in the IR has to accommodate this situation. Also, attention must be paid to possible trapping of higher order mode (HOM) RF fields in this area. Although efforts are being made to reach an optimum solution, some amount of HOM trapping, and heating due to it, will be inevitable. To rectify this situation, the possibility of implementing some antenna structures to remove the HOM power from this section is being contemplated.

7.4 Superconducting Magnets for IR

7.4.1 Introduction

Four superconducting magnets will be used in the interaction region: solenoid field compensation magnets (S-L and S-R), and final focusing quadrupole magnets (QCS-L and QCS-R). Each pair of S + QCS magnets in the left and right side is contained in a single stainless steel vessel. It provides a sturdy structure which tightly holds the coil windings and prevents their motions during cooling down and excitation. The vessels (cryostat) are designed to withstand forces due to the magnetic field of the coils, themselves, and their interactions with the detector solenoid field. They have to be installed completely inside the detector facility. Figure 7.4 shows the layout of the interaction region with the superconducting magnets, surrounded by the detector elements. This section presents the engineering design work that has been done for the superconducting magnets.

7.4.2 Compensation solenoids

The two field compensation solenoids have magnetic fields opposite to the detector solenoid. Figures 7.5(A) and 7.5(B) show cross section views of the right and left solenoids in their horizontal cryostats. In both cases, the solenoid coil has an inner diameter of 190 mm, and a thickness of 15 mm. Between the inner helium vessel and

	S-R	S-L	
Central field	5.4	4.4	T
Coil current density	300	258	A/mm^2
Coil			
Inner diameter	190	190	mm
Outer diameter	220	220	mm
Length	650	470	mm
Max. field of the conductor	5.4	4.5	T
Stored energy	225	115	kJ
Magnetic pressure in radial direction	9.2	6.4	MN/m^2

Table 7.5: Main parameters for the solenoid magnets.

the coil, some space is allocated for accommodating a few kinds of correction coils. The main parameters of these solenoids are listed in Table 7.5. The final specifications of the conductor wire and the operating current will be decided in the near future, while tacking into account the magnetic coupling with the detector solenoid and the heat load to the cooling system.

A computer code OPERA-2D has been used to calculate the magnetic field from the combination of those solenoid magnets, the detector solenoid, and its field return yoke structure. Figure 7.6 shows the expected axial magnetic field B_z along the beam axis. With this configuration, the integral of B_z along the accelerator beam line is brought to zero.

The field distortions in the detector's tracking volume, which is caused by the leak field from these solenoids, have been evaluated. Figure 7.7 shows the contour lines of the field distortions relative to the nominal 1.5 T solenoid field. The number attached to each contour line indicates the field deviation expressed in the unit of percent. Except for the regions close to the compensation solenoids, the field deviation in the volume for charged particle tracking by the experimental facility is less than 5%. According to simulations studies carried out by the detector group, this is considered to be acceptable.

When the solenoid magnets are excited in the detector field, axial magnetic forces which act on the solenoid coils appear. The peak field values on the conductor will be shifted from the values in Table 7.5. These effects have also been evaluated using OPERA-2D. The estimated magnetic forces are listed in Table 7.6. The axial body force that acts on the S-L coil is 22 kN. Although it is somewhat large, it is well within

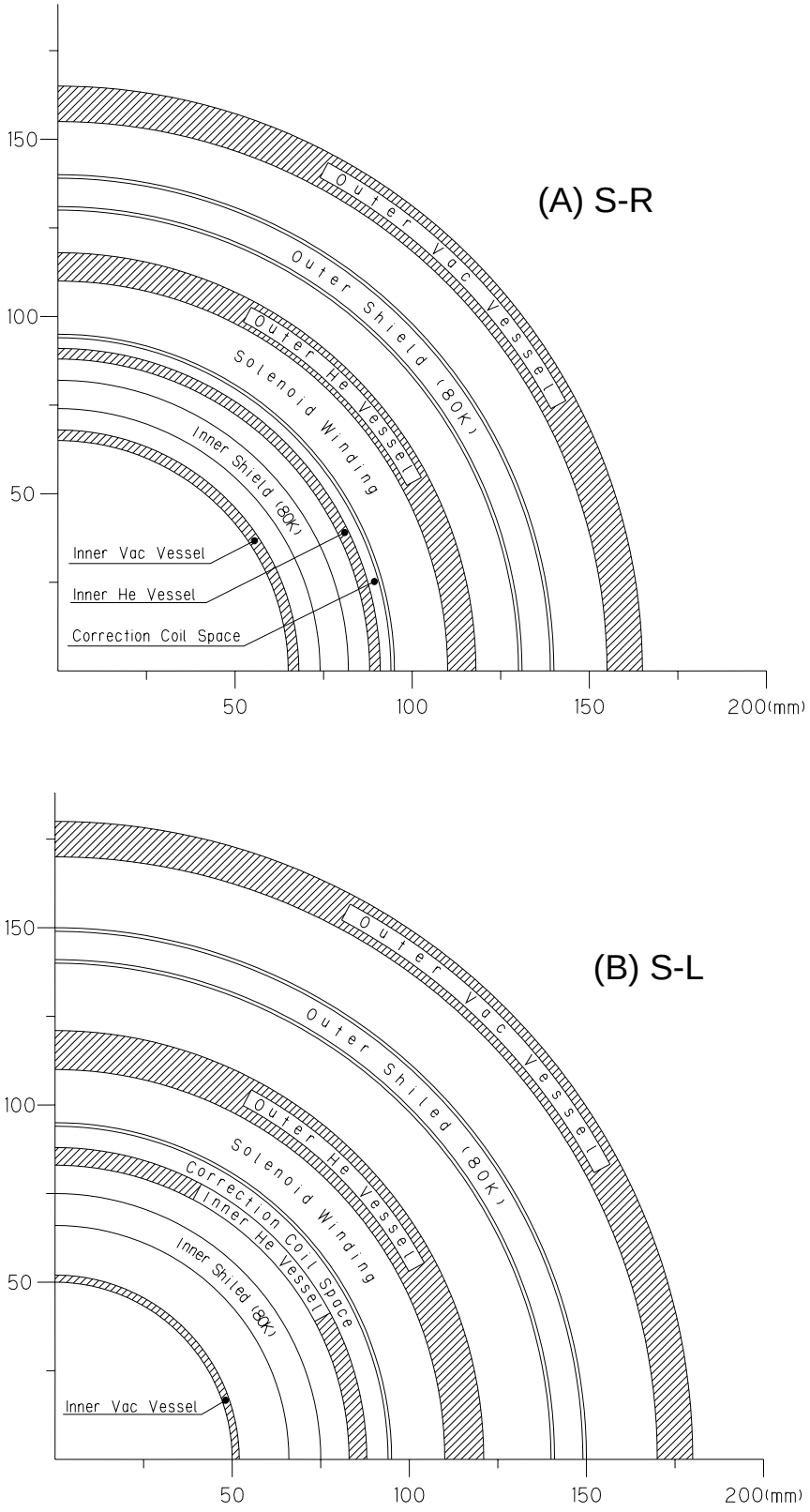

Figure 7.5: Cross section views of the S-R solenoid (A) and the S-L solenoid (B).

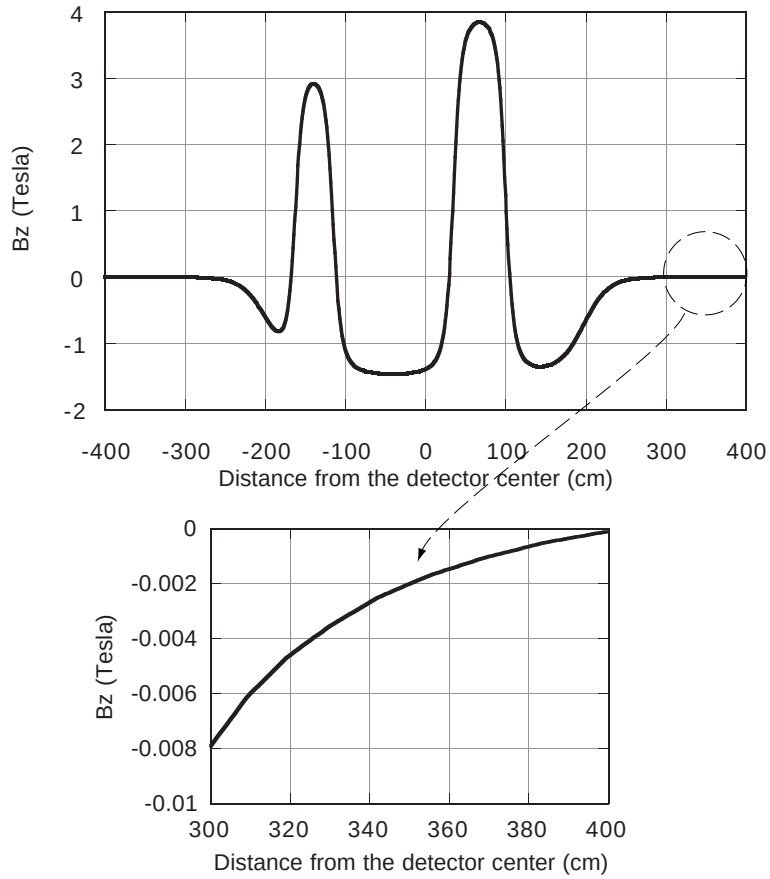

Figure 7.6: Distribution of the axial magnetic field B_z along the axis of the experimental facility.

	S-R	S-L	
Magnetic pressure			
in radial direction	3.1	1.4	MN/m^2
Body force			
in axial direction	2.8	22	kN

Table 7.6: Pressure and force on the solenoids placed in a 1.5 Tesla detector solenoid.

the acceptable level from engineering viewpoints. The maximum field strength on the conductors of both solenoids are decreased by 1.5 T, due to the opposite sign of the detector field.

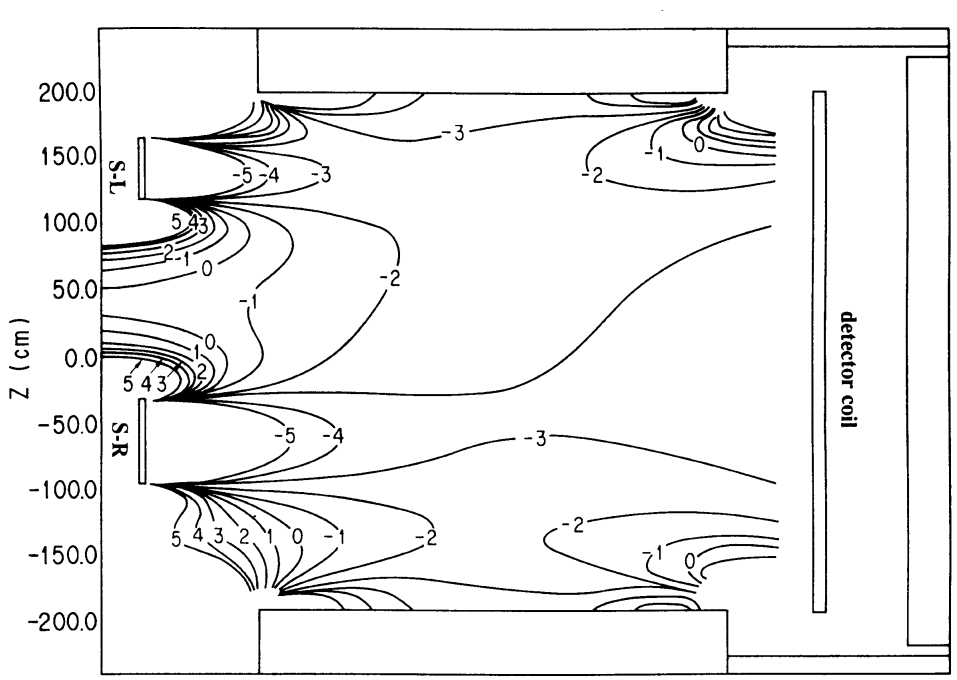

Figure 7.7: Contour lines of the field distortions relative to the nominal 1.5 T solenoid field. The number attached to each contour line indicates the field deviation expressed in the unit of percent.

Field gradient	18.8	T/m
Current	2224	A
Coil		
Inner diameter	260	mm
Outer diameter	295.4	mm
Overall length of the coil	780	mm (for QCS-L)
	710	mm (for QCS-R)
Collars		
Material	SUS316LN	
Radial thickness	27	mm
Integrated field uniformity (at $r = 40$ mm)		
B_6L/B_2L	$< 1 \times 10^{-4}$	
$B_{10}L/B_2L$	$< 1 \times 10^{-4}$	
Effective magnetic length	490	mm (for QCS-L)
	420	mm (for QCS-R)
Max. field on the conductor	3.1	T
Stored energy	157	kJ
Magnetic force per unit length in a coil octant		
F_x (horizontal)	125	kN/m
F_y (vertical)	-290	kN/m

Table 7.7: Parameters of the superconducting quadrupole magnet. The overall length of the coils does not include the coil end spacer and magnet end plates.

7.4.3 Quadrupole magnets

The final quadrupole magnets are iron-free, superconducting magnets. They provide a maximum field gradient of 18.8 T/m for an effective field length of 0.5 m in a usable aperture diameter of 80 mm. Extensive experience from the development, fabrication and operation of the TRISTAN superconducting mini-beta insertion magnets is reflected in the design work.

The basic design of QCS is similar to that of the TRISTAN magnets. It is based on a set of $\cos 2\theta$ winding layers clamped by stainless steel collars. The required warm bore aperture specifications of QCS-R and QCS-L are approximately the same. This allows us to use an identical coil structure for both sides, QCS-L and QCS-R. However, the dimensions of the cryostats will be different, as discussed in a previous section. The main parameters of the quadrupole magnet are listed in Table 7.7.

Cable dimensions		
width	8.35 ± 0.05	mm
thickness	0.925 ± 0.02	mm
Number of SC strands	16	
Number of Cu strands	16	
Cu / SC ratio of SC strand	2.0	
Strand diameter	0.510 ± 0.005	mm
Filament diameter	< 6	μm
RRR of stabilizing copper	180 ± 20	
Cable twist pitch	70 ± 5	mm
Critical current in cable (at 4.2 K)		
	more than 2900	A at 5T
	more than 4200	A at 3T

Table 7.8: Parameters of the superconducting cable.

Figure 7.8(A) shows a cross section of the QCS-R magnet in a horizontal cryostat. The inner diameter of the warm bore is 178 mm, and the outer diameter of the vacuum vessel is 480 mm. Starting with the innermost part, the main components of the magnet are: a warm bore, inner radiation shield, inner wall of the helium vessel, correction coils, main coil, stainless steel collar, outer wall of the helium vessel, outer radiation shield and vacuum vessel.

The main coil is made of two layers of superconducting windings. The $\cos 2\theta$ current distribution is approximated by using a copper wedge in the first layer. To keep the higher multipole fields within the tolerances, a computer code based on an analytical formula of field harmonics has been used to determine the two-dimensional cross section of the coil winding. The resultant shape has 115 turns in total, combining the first and second layers in each of the four quadrants. The operating current was chosen to be relatively small. This allows us to reduce the heat load on the cooling system.

The superconducting cable will be of the NbTi/Cu Rutherford type, which is commonly used in many accelerator magnets. Since the operating current is relatively low, it is planned to use a cable in which copper strands and NbTi/Cu strands are mixed for ease of the winding process. The main parameters of the cable are listed in Table 7.8.

Effects of various fabrication errors of the coils have been investigated. A basic eight-fold symmetry in the coil geometry is assumed. Table 7.9 summarizes the results of this study. The quoted numbers are for a 0.1 mm variation of the parameters listed.

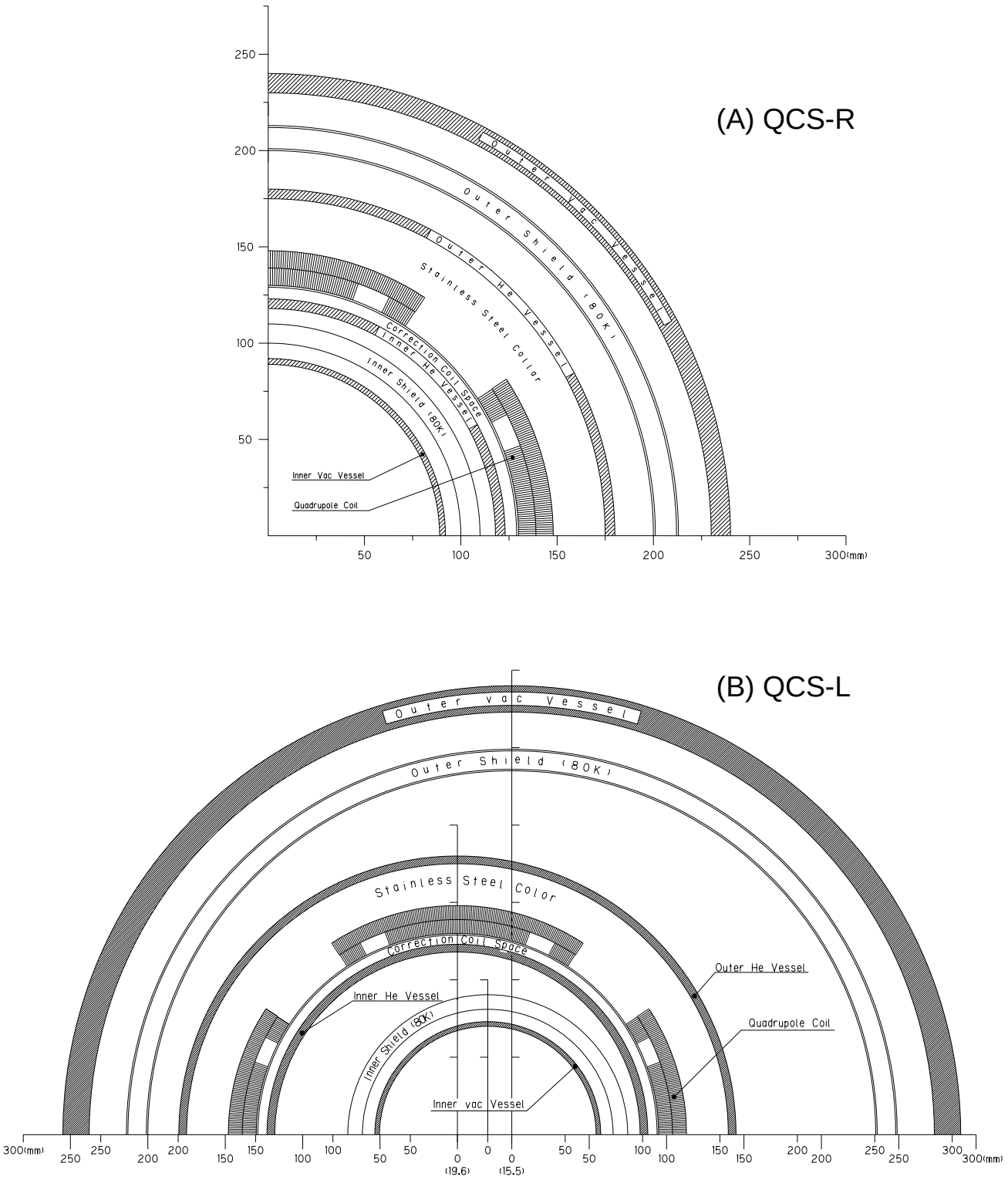

Figure 7.8: Cross section views of the QCS-R (A) and QCS-L (B) magnets.

Parameters changed	b_2 (mT/m)	b_6 10^{-4}	b_{10} 10^{-4}
Radius of inner coil	−11.0	−0.14	−0.00
Radius of outer coil	−32.6	−0.10	−0.00
Radius of inner No.1 coil	−9.41	−0.18	−0.00
Radius of inner No.2 coil	−4.73	−0.07	−0.00
Pole angle of inner coil	−4.96	−0.11	−0.00
Pole angle of outer coil	−19.0	−0.17	−0.00
Wedge of inner coil	−4.22	−0.20	−0.00

Table 7.9: The values show the effect of a 0.1 mm shift of the given parameter on the quadrupole field strength and higher harmonics at $r = 40$mm.

The harmonics are calculated at a reference radius of 40 mm.

Since the quadrupole magnets considered here are rather short compared to other typical accelerator superconducting magnets, the effects of the end parts are not negligible. Three-dimensional field calculations are in progress to investigate the field distribution, and to optimize the shape of the coil end.

Figure 7.8 shows a cross section of the QCS-L magnet in the horizontal cryostat. In this case, the quadrupole axis has to be shifted horizontally by 35.1 mm from the detector axis. Therefore, the cryostat has a rather complex structure, as shown in the figure. However, the engineering work for fabricating this magnet is considered to be quite possible. In this eccentric configuration, higher order multipole fields and the asymmetric electromagnetic forces can arise, due to the image current in the end yoke of the detector. An estimate of this effect has been made by treating the issue as a 2-dimensional problem. Beam dynamics calculations based on this estimate have found that the higher multipole fields are well within an acceptable level in terms of dynamic apertures. The strength of the attractive force between the end yoke and the quadrupole magnet is about 2.3 kN, which is within a manageable range.

7.4.4 Cryostat and cooling system

As mentioned earlier, two cryostats will be built and installed on each side of the interaction point. A preliminary design of these cryostats has been conducted, while taking into account the many practical constraints near the interaction point. They include: the desire for a small outer diameter, a narrow thermal insulation space, sufficient mechanical strength to sustain the forces acting on the magnets, a small heat load, and others. The longitudinal cross sections of these cryostats, including the

Cryostat	(including connection box)	35 W ×2	
Current leads			
	for QCS-R and QCS-L		11 ℓ/h
	for S-R and S-L		7 ℓ/h
	for six kinds of correction coils		9.5 ℓ/h
Transfer line	$\sim$ 35 m	56 W	
	(including 2 connection boxes)		
Subcooler		6.6 W	
	Total	97.6 W	+27.5 ℓ/h

Table 7.10: Estimated heat load and the required amount of liquid helium for the QCS cryogenic system.

coils, the radiation shield, and the helium vessel, are shown in Figures 7.9(A) and (B). Detailed designs of the support rods and piping are in progress. The heat load of a pair of cryostats is estimated to be less than 35 W.

The estimated head load of each cryogenic component is listed in Table 7.10. Allowing for a minimum safety margin of 2.1, the required capacity of the common refrigerator is 203 W + 27.5 ℓ/h. The cooling system that has been used for the Tristan mini-beta insertion quadrupole magnets since 1991 has a capacity of that level. It will, therefore, be recycled and reused. The basic components of the system (helium compressor, cold box, sub-cooler, and control computer) will be reused. Figure 7.10 shows a simplified flow diagram of this system. The system will use single phase liquid helium of 4.5 K and 0.16 MPa.

7.5 Special Quadrupole Magnets for IR

Near the interaction point, six iron-dominated quadrupole magnets of special type are required: QC2E-L, QC1E-L, QC1E-R and QC2E-R for HER, and QC2P-R and QC2P-L for LER. The specifications for these quadrupole magnets are listed in Tables 7.11 and 7.12.

The purpose of these magnets is to apply optimized focusing and defocusing fields on electrons and positrons, independent of each other. Figure 7.11 shows the areas occupied by beams of electrons and positrons and their center positions at the edges of QC1E-L and QC2P-R. The ellipses indicate the beam areas which correspond to the beam envelope during the injection time, plus the vacuum chamber thickness 5 mm.

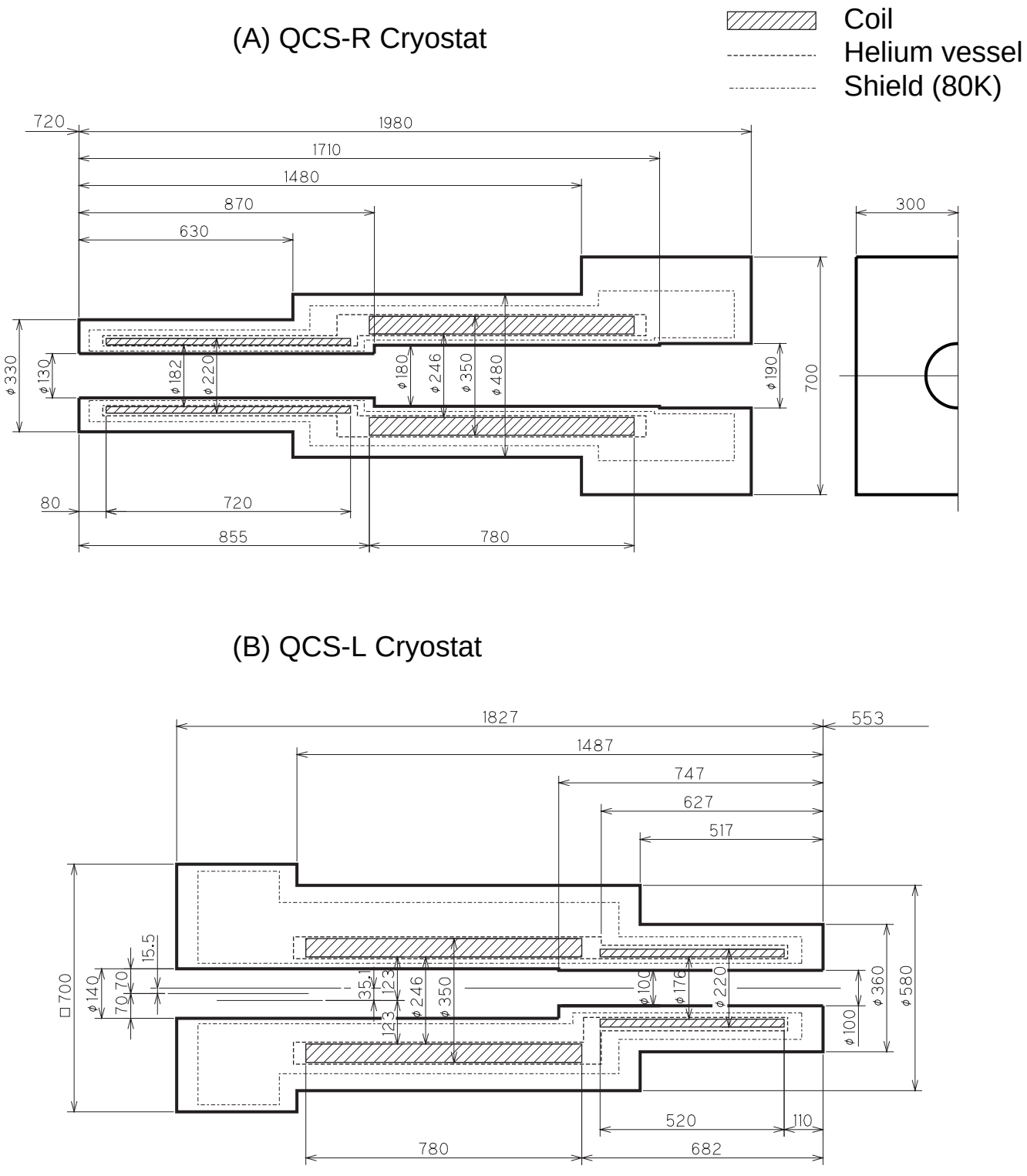

Figure 7.9: Longitudinal cross section views of the right-side cryostat (A) that contains S-R and QCS-R, and the left-side cryostat (B) that contains S-L and QCS-L. The dimensions are given in mm.

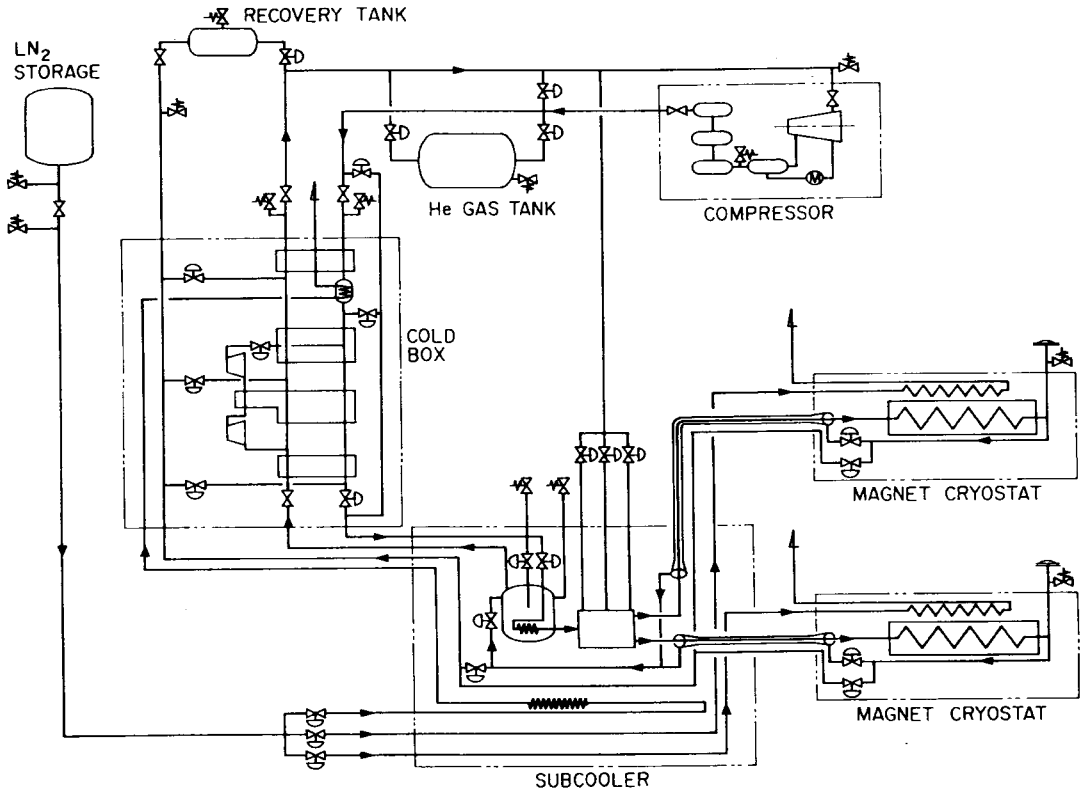

Figure 7.10: Simplified flow diagram of the helium cooling system.

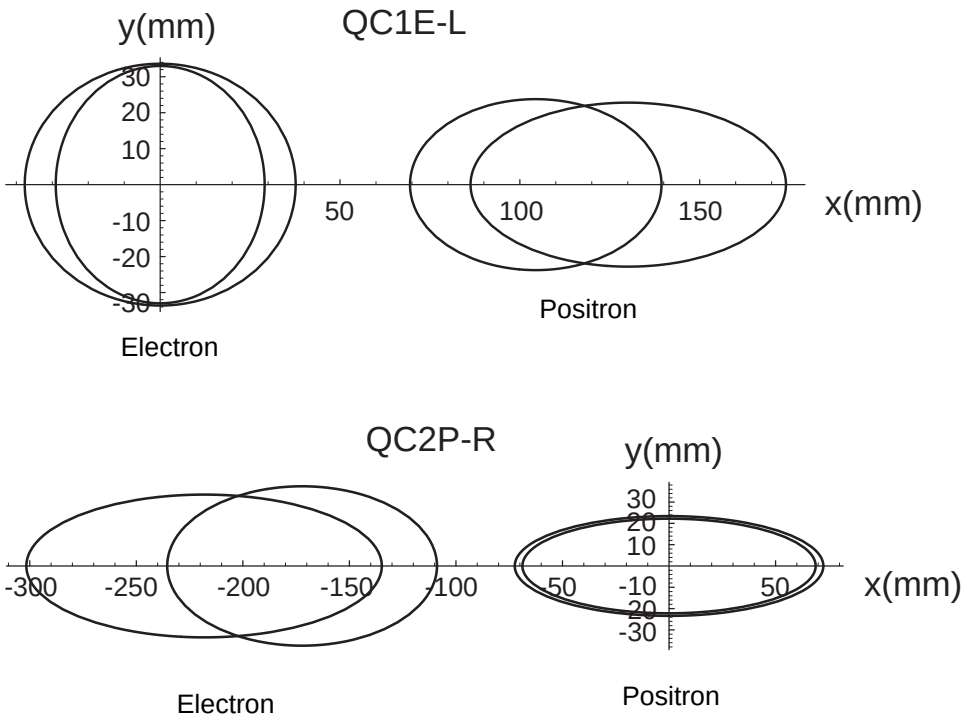

Figure 7.11: Beam positions and beam envelopes during the injection time at the edges of QC1E-L and QC2P-R.

		QC1E-L	QC2E-L	QC1E-R	QC2E-R
Entrance aperture(e^-)	horizontal(mm)	37.66	114.7	38.47	99.5
	vertical(mm)	33.62	18.5	39.85	30.4
Exit aperture(e^-)	horizontal(mm)	29.04	106.7	47.27	105.2
	vertical(mm)	32.99	20.4	40.43	29.8
Entrance aperture(e^+)	horizontal(mm)	43.85	50.9	48.1	61.5
	vertical(mm)	22.8	33.9	24.5	29.2
Exit aperture(e^+)	horizontal(mm)	34.96	53.1	56.95	66.2
	vertical(mm)	23.77	30.8	23.51	26.7
Beam separation	entrance(mm)	130.14	339.0	112.2	254.8
Beam separation	exit(mm)	100.42	302.0	132.2	283.0
Max. field gradient	(T/m)	15.4	6.1	12.6	10.2
Pole length	(m)	0.6	1.0	0.6	0.6

Table 7.11: Specification of the IR quads for HER.

		QC2P-L	QC2P-R
Entrance aperture(e^-)	horizontal(mm)	52.99	63.3
	vertical(mm)	30.69	37.4
Exit aperture(e^-)	horizontal(mm)	64.51	83.4
	vertical(mm)	28.48	33.5
Entrance aperture(e^+)	horizontal(mm)	55.7	68.8
	vertical(mm)	21.52	22.2
Exit Aperture(e^+)	horizontal(mm)	59.37	72.4
	vertical(mm)	22.19	23.4
Beam separation	entrance(mm)	170.0	172.2
Beam separation	exit(mm)	200.0	218.2
Max. field gradient	(T/m)	7.3	4.1
Pole length	(m)	0.6	1.0

Table 7.12: Specifications of the IR quads for LER.

The beam emittance envelope of $\varepsilon_x = 1.4 \times 10^{-5}$m and $\varepsilon_y = 1.4 \times 10^{-6}$m is assumed for the beam during the injection time. The beam line has been designed to create a sufficient beam separation within those magnets, so that magnets with realistic engineering design can be built. Five of these magnets will be built as full quadrupole magnets. They have to have non-standard shapes in which a field free space is embedded for the beam of the other ring. Due to the limited beam separation, one of them, QC1E-R, will have to be a half quadrupole magnet.

Although a large region with good field quality must be created, in the region for the other beam ("spectator beam") the field strength must be minimized. This has to be achieved while the beam separation is only marginal. For example, the free space thickness for QC1E-L and QC2P-R is merely $30 \sim 40$ mm. Consequently, the thickness of the conductor in between must be minimized. The conductor shape resembles that of a septum magnet. Therefore, QC1E-L and QC2P-R will have very high current density in the conductors. The field distribution in those magnets have been calculated using the computer code Poisson. The cross section shapes of QC2E-L, QC2P-R, QC1E-L and QC1E-R have been determined, as shown in Figure 7.12.

The magnet that has the highest current density in the coil is QC1E-L; the overall current density of its "septum conductor" is about 56 A/mm^2. Although not trivial, it is considered to be possible to cool the conductor by minimizing the length of the cooling circuit. It is considered relatively easy to build QC2E-R and QC2P-L, because

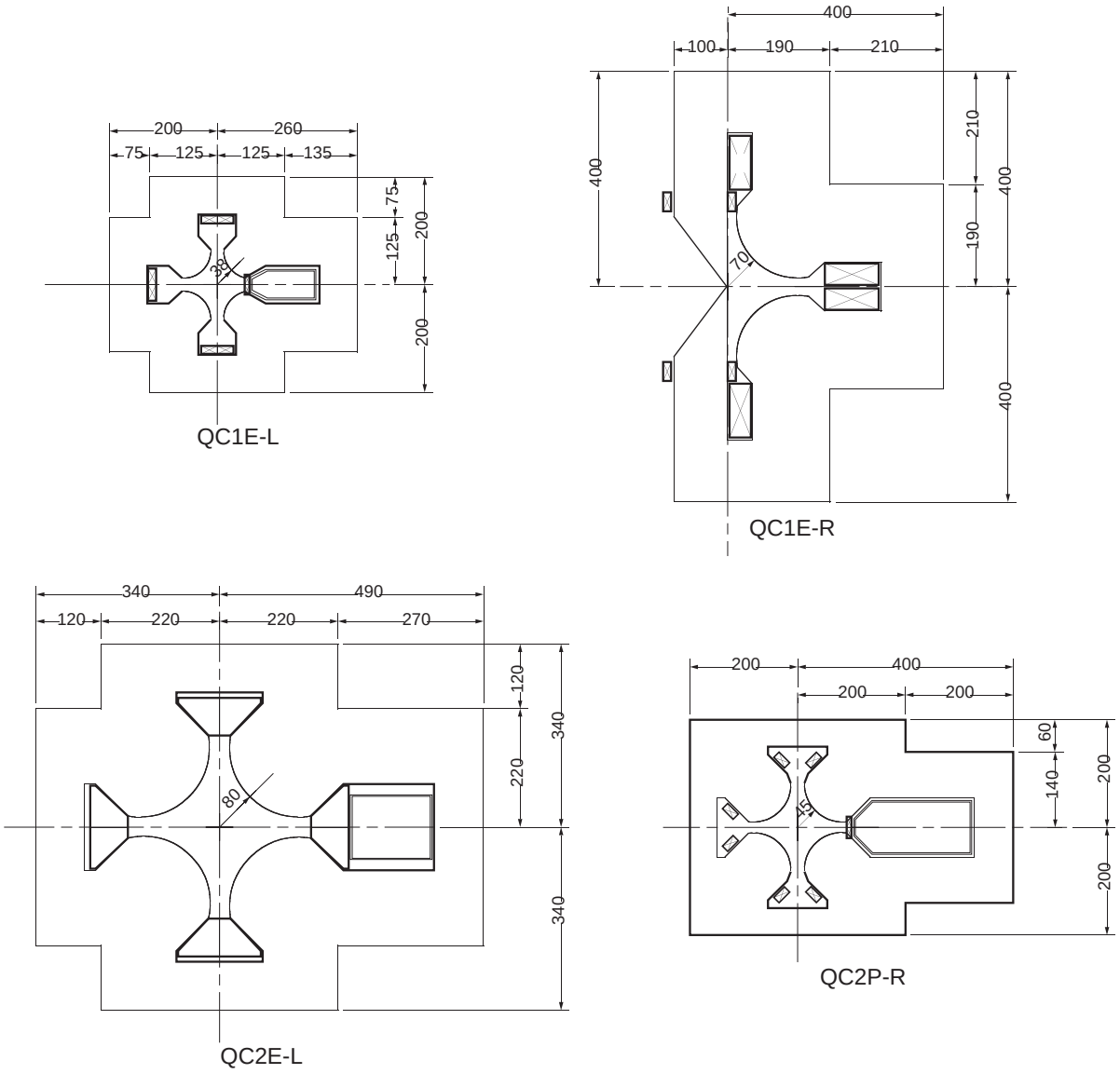

Figure 7.12: Cross section shapes of some of the special IR quadrupole magnets.

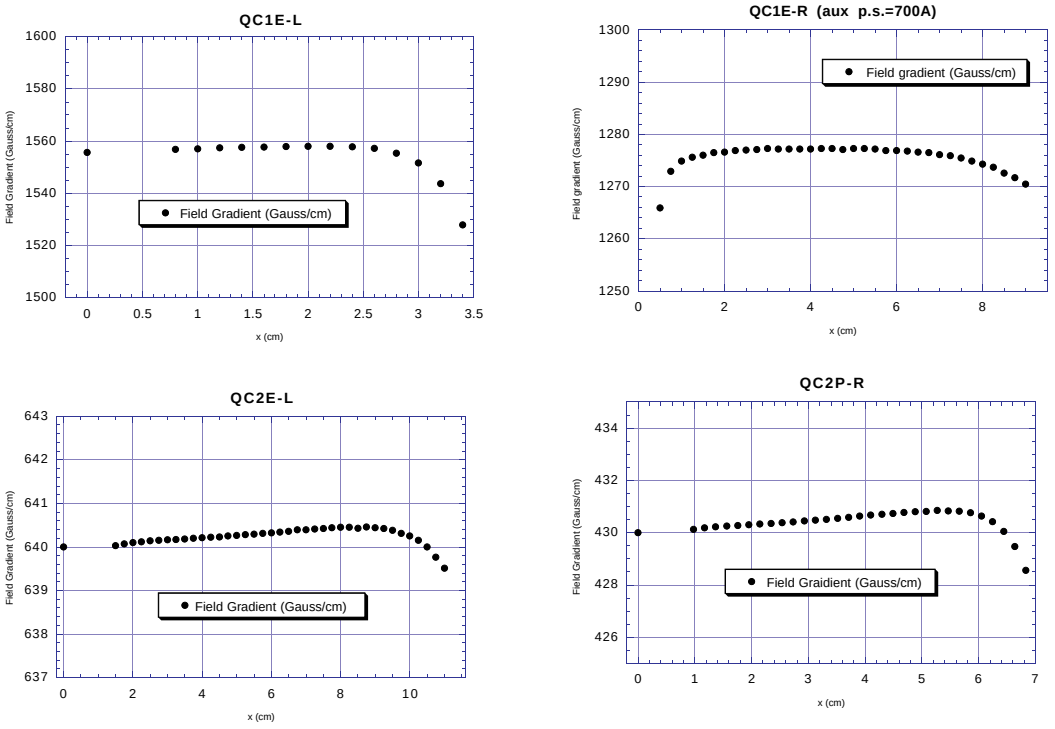

Figure 7.13: Calculated distributions of the field gradient of the IP quads.

the free space between two beam areas is much larger. Since the field distribution near the pole edge is also affected by the position of the conductor, it is important to mechanically firmly fix the "septum conductor" against its thermal expansion and magnetic forces.

As for the half quad (QC1E-R), the field distribution near the iron septum is determined by a delicate relation between the magnetic resistance of the flux circuits. To make corrections for possible errors, trim coils will be attached to the iron septum.

The calculated field gradient distributions of QC2E-L, QC2P-R, QC1E-L and QC1E-R are shown in Figure 7.13. If a further reduction of the field gradient near the aperture boundary is proved necessary, this can be done, to some extent, by adding end-shims. Because of the lack of 90-degree rotation symmetry, this magnet geometry is prone to produce sextupole and octapole fields due to errors. If these multipole components are found to be larger than the tolerance, a magnet geometry with a 90-degree rotation symmetry may have to be implemented. Investigations of these possibilities will be made in the near future, before freezing the final design of these magnets. The parameters of four of six IR special quads are listed in Table 7.13.

	QC1E-L	QC1E-R	QC2E-L	QC2P-R
Aperture radius(mm)	38	70	80	45
Pole length(m)	0.6	0.6	1.0	1.0
Max. field gradient(T/m)	15.6	12.7	6.4	4.3
Current(AT)	9000	27000	16500	3500
Current density of the septum conductor(A/mm^2)	56	6.8	4.6	22
Field in the area for counter-circulating beam (with magnetic shield)(Gauss)	$0 \sim -1$	$0 \sim -2$	$2 \sim -0.6$	$0 \sim -1$

Table 7.13: Parameters of QC1E-L, QC1E-R, QC2E-L and QC2P-R.

7.6 Installation and Magnet Support for IR

The magnets which will be placed in the Tsukuba experimental hall (IR hall) are superconducting magnets in the QCS solenoids, QC1E, QC2E and QC2P magnets. The support structure of the QCS cryostat is illustrated in Figure 7.14. The QCS cryostats are supported from a movable stage. This movable stage serves as a common support base for other accelerator magnets (QC1 and QC2 for both the LER and HER) located in the IR hall.

The movable stage can move along the beam line by approximately 4 m. The QCS magnets can be pulled out and pushed in with this motion. The alignment position and angle of the QCS cryostats can be adjusted by a mechanism installed on the support base. The relative positions between the cryostat and the endcap calorimeters are monitored by four units of a position measurement device called "holo-gauge." These gauges have been tested to be operational in a high magnetic field up to 1 T with radiation dose up to 10 krad.

In order to prevent vibration of the QCS head during an earthquake, movement of the cryostat body is limited by four support bars which are stretched radially from the support rails of the endcap calorimeter. When the QCS cryostat or the endcap calorimeter needs to be moved, the support bars are mechanically moved, and its connection to the cryostat is loosened. This allows the cryostats to slip off the support bars. When the cryostat is to be stationed in the operational location, the cryostat body is latched to the support bars.

To align the left and right QCS magnets, hair cross targets are installed on the

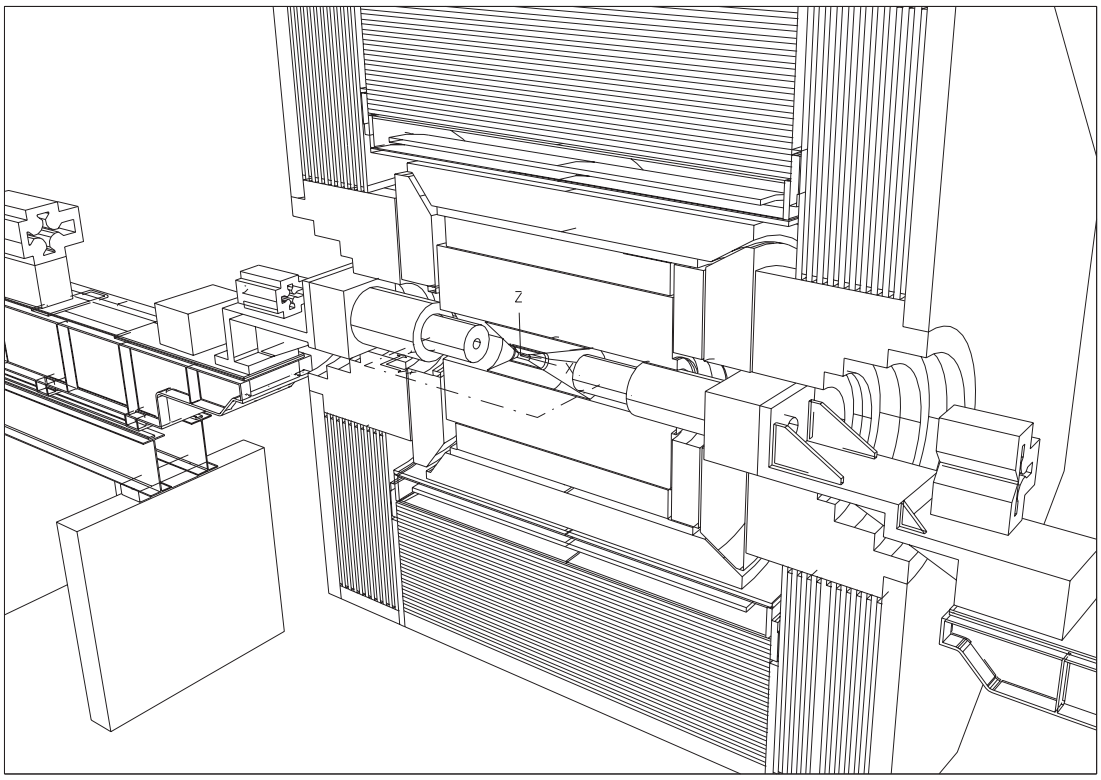

Figure 7.14: The QCS cryostats and other IR special magnets placed near the IP. A cut-away view of the detector facility is also shown.

surface of each QCS cryostat. The targets are grouped in two pairs, each of which determine the horizontal and vertical position of the cryostats. On each endplate of the central drift chamber, two quartz windows with a radius of ~ 7 mm will be installed. They will allow the surveyors to look through the left and the right pair of targets. This way, the pair of QCS magnets can be aligned within 0.1 mm. Then, the position of the QCS pair can be used as a reference to connect the beam lines on both sides of the detector.

The cryogenic transfer tubes, which deliver the superconducting power cables and liquid coolant from the outside connection boxes to the cryostat, will have an outer diameter of 26 cm. Its routing in the neighborhood of the crowded beamline near the IP has been studied. A workable solution has been found. Details concerning installation procedures for the entire beam line near the IP, including the cryostats, vacuum components and transfer tubes, are being worked out.

Magnets beyond QC2s will reside in the straight section tunnels next to the IR hall. Figure 7.15 shows a schematic plan view of the beam line near the IR hall.

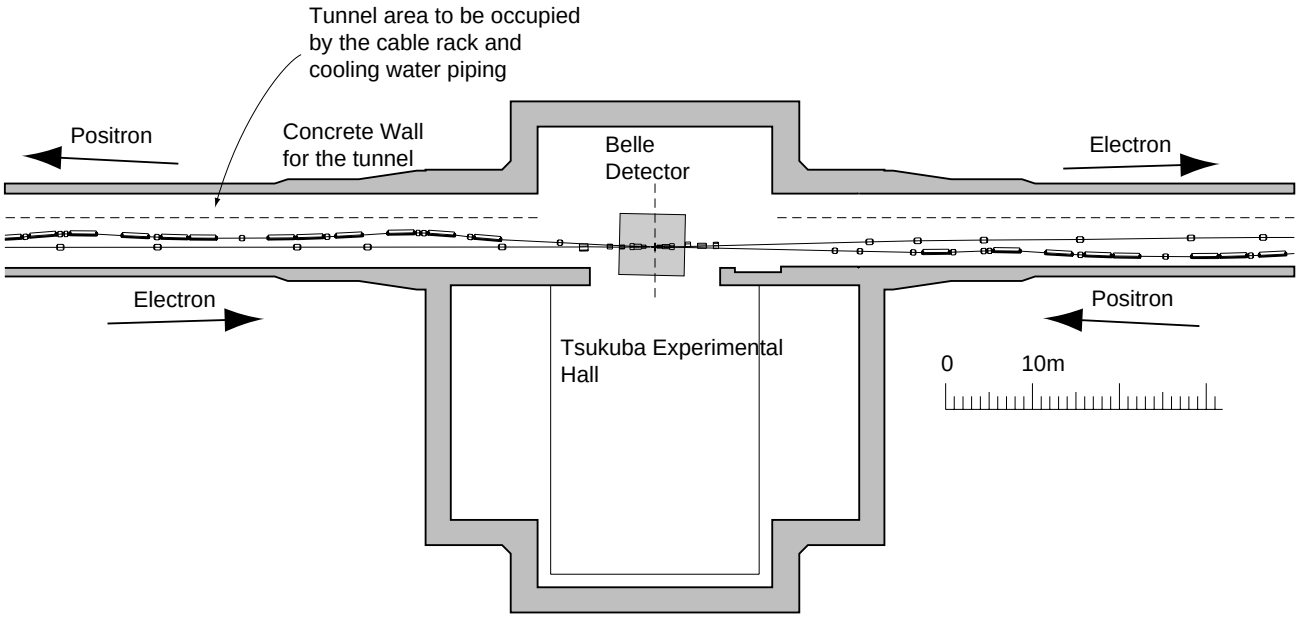

Figure 7.15: Schematic plan view of the beam line near the IR hall. The LER and HER beams collide at the interaction point within the detector facility, called "Belle." The concrete walls for the tunnels are included. The beam line components are not allowed to extend into the tunnel area that will be occupied by the cable rack and cooling water piping. The allowed boundary is indicated by broken lines.

7.7 Beam Background

7.7.1 General

Since a finite crossing angle scheme is adopted, and separation bend magnets will no longer be used, the conditions to consider the background issues have become much more relaxed than the past case which is described was the detector reference design in 1994 [1] [2]. Still, much detailed simulation work is required before freezing the final design of the masking system. This section briefly outlines the strategies used for handling synchrotron radiation (SR) and the particle background near the IP.

A high precision charged particle tracking device with silicon micro-strips will be installed, surrounding the IP. The requirement on the momentum resolution of the tracking system calls for using a cylindrical beam pipe with an inner diameter of 40 mm for $-80 < z < +80$ mm. This beam pipe will be made of a double-wall beryllium structure for efficient cooling with a minimum amount of material. At the edge of this beryllium central vacuum pipe, Mask-A will be implemented so that the Be pipe is shielded from back-scattered photons. The arrangement of the beryllium pipe and Mask-A are illustrated in Figure 7.16. Mask-A and vacuum chambers outside will be made of copper.

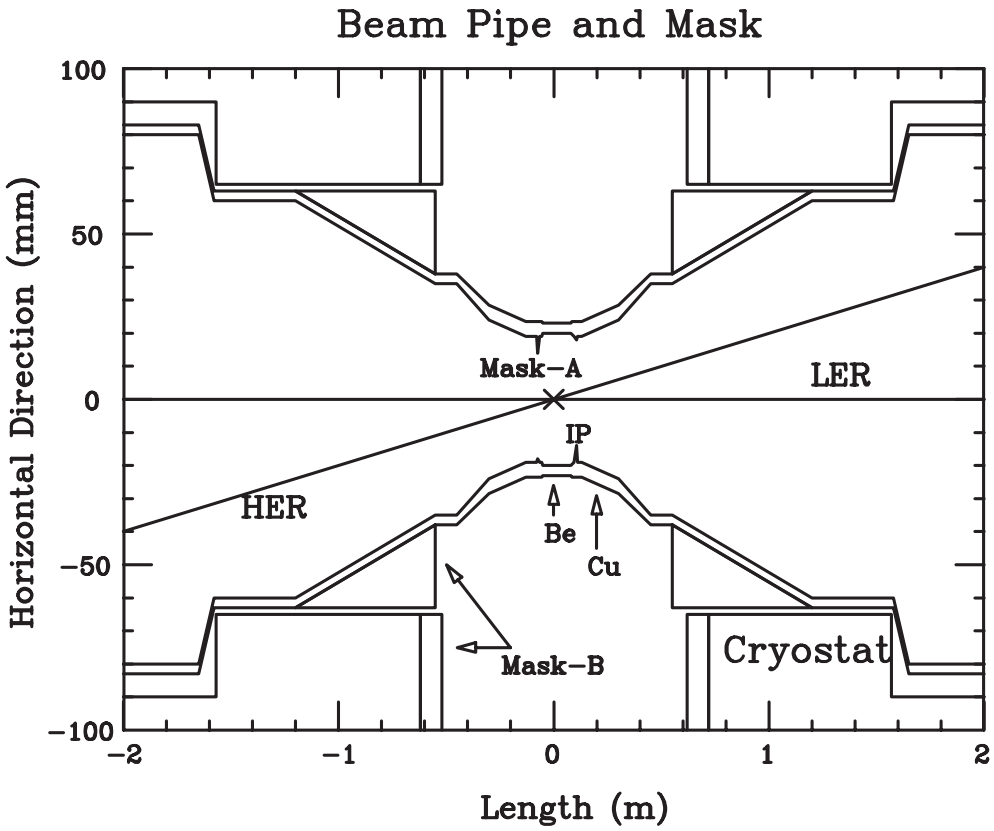

Figure 7.16: Arrangement of the central beam pipe at the IP and horizontal masks

7.7.2 Synchrotron radiation

The SR from bunch particles going through QCS and QC1 are required not to directly hit the Be pipe and Mask-A. The geometry of the magnet layout in the IR and their excitations have been chosen so that this requirement is satisfied. Calculations have shown that if the fractional particle population beyond $10\sigma_x$ and $30\sigma_y$ is kept below 10^{-5}, the SR background should have no significant harmful effects for data acquisition and analysis. Simulations of bunch tail development indicate that this condition will be met.

Some of the photons from upstream magnets QC2 and QC3 can hit Mask-A. Since those photons will have a critical energy below 2 keV, they can be easily absorbed by heavy metal. The masks and the inner surface of vacuum chambers will be gold-plated for this purpose. Photons from far upstream magnets away from the IP should be intercepted by movable masks installed just upstream of QC3. The design of these movable masks will soon be started.

7.7.3 Particle background

The particle background is, again, expected to be less severe than in the case of the past reference design. In the presence of separation bend magnets, the low-momentum charged particles could be easily swept into the detector. This is no longer the case with the finite-angle crossing scheme. However, the particle background can be potentially more serious than the SR background.

Calculations by the computer code Decay Turtle have been done. It has been found that the rate of spent particles from the two beams to directly hit the beam pipe between the two cryostats is 130 kHz, when the vacuum pressure is 10^{-9} torr. (This rate is a factor of three smaller than that for the past reference design.)

According to the simulation, the vacuum pressure outside QC2 is more important than that inside the detector, where the pumping speed is limited by the beam pipe aperture. The best efforts will be made to implement efficient pumping systems near QC2 magnets. The design goal for the vacuum level in the region outside QC2 is 10^{-10} torr.

Mask-B (shown in Figure 7.16) will be installed outside of the beam pipe to reduce the particle background. Movable masks should be installed in the arcs and the non-IR straight sections to clip the beam tails. They will help reduce the radiation level at the detector facility during the injection time. Detailed design work of these mask systems will start soon.

Bibliography

[1] The BELLE Collaboration, KEK Report 94-2, 1995. p. 58.

[2] BELLE Collaboration, Technical Design Report, KEK Report 95-1, 1995.